Timing methodologies and studies at the FERMI free-electron laser

Riccardo Mincigrucci,[a]* Filippo Bencivenga,[a] Emiliano Principi,[a] Flavio Capotondi,[a] Laura Foglia,[a] Denys Naumenko,[a] Alberto Simoncig,[a] Simone Dal Zilio,[b] Alessandro Gessini,[a] Gabor Kurdi,[a] Nicola Mahne,[a] Michele Manfredda,[a] Alessia Matruglio,[c] Ivaylo Nikolov,[a] Emanuele Pedersoli,[a] Lorenzo Raimondi,[a] Rudi Sergo,[a] Marco Zangrando[a,d] and Claudio Masciovecchio[a]

[a]Elettra Sincrotrone Trieste SCpA, Strada Statale 14, km 163.5 in AREA Science Park, Basovizza 34149, Italy, [b]IOM Laboratorio Nazionale TASC, Strada Statale 14, km 163.5 in AREA Science Park, Basovizza 34149, Italy, [c]CERIC-ERIC (Central European Research Infrastructure Consortium), Strada Statale 14, km 163.5 in AREA Science Park, Basovizza 34149, Italy, and [d]CNR_IOM, Laboratorio TASC, Strada Statale 14, km 163.5 in AREA Science Park, Basovizza 34149, Italy. *Correspondence e-mail: riccardo.mincigrucci@elettra.eu

Time-resolved investigations have begun a new era of chemistry and physics, enabling the monitoring in real time of the dynamics of chemical reactions and matter. Induced transient optical absorption is a basic ultrafast electronic effect, originated by a partial depletion of the valence band, that can be triggered by exposing insulators and semiconductors to sub-picosecond extreme-ultraviolet pulses. Besides its scientific and fundamental implications, this process is very important as it is routinely applied in free-electron laser (FEL) facilities to achieve the temporal superposition between FEL and optical laser pulses with tens of femtoseconds accuracy. Here, a set of methodologies developed at the FERMI facility based on ultrafast effects in condensed materials and employed to effectively determine the FEL/laser cross correlation are presented.

1. Introduction

During the past 30 years, the advent of pulsed lasers enabled the scientific community to explore physical processes in a time-resolved manner. Generally, in time-resolved 'pump–probe' experiments a laser pulse is split, eventually optically manipulated and recombined onto the sample with a relative time delay (Borrego-Varillas *et al.*, 2016; Kruglik *et al.*, 2011; Cucini *et al.*, 2007). In such schemes, one of the two pulses can act as a pump, triggering the dynamics of the system under investigation, while the second one, properly delayed, probes the temporal evolution of the activated dynamics. The list of the accessible phenomena is vast, *e.g.* ultra-fast melting (Beye *et al.*, 2010), chemical reactions (Kowalewski *et al.*, 2015), electronic and magnetic dynamics (Gutt *et al.*, 2017) and acoustic dynamics (Cucini *et al.*, 2011*a*) to cite only a few experiments performed at free-electron laser (FEL) facilities. Independent of the investigated physics, before performing any pump–probe experiment, the pump and probe beams have to be spatially superposed and the time instant (t_0) when the pulses are temporary overlapped has to be determined. Failure in the identification of t_0 or the inability to measure it shot-by-shot in jittering sources, prevents any kind of studies or, even worse, can introduce severe artefacts in the measurements (Harmand *et al.*, 2013). A quick and effective strategy to determine t_0, especially in FEL facilities, where the experimental time is costly, is tremendously advisable. In this work, we present some timing strategies tailored to the focal
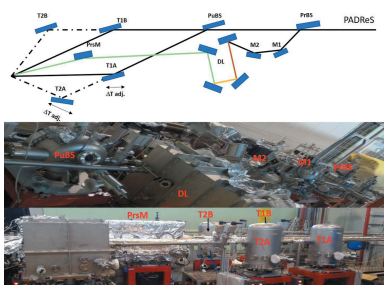
spot characteristics of three different FEL endstations (EIS-TIMEX, EIS-TIMER and DiProI) of the Italian FEL facility FERMI (Allaria *et al.*, 2012).

2. EIS-TIMEX

The main scientific objective of EIS-TIMEX is the study of matter under extreme and metastable conditions, with special focus on non-equilibrium and warm dense matter (WDM) regimes. Non-equilibrium condensed matter occurs just upon intense laser pulse exposure and it is characterized by a hot electron subsystem (more than a few eV, 1 eV = 11.6×10^3 K) and a room-temperature ion lattice.

After a few hundred femtoseconds, electrons and ions isochorically thermalize, possibly leading the condensed material in a WDM phase (density: 5–10 g cm^{-3}; temperature: greater than 1 eV). WDM conditions are believed to exist in a steady state regime in large planet interiors and external regions of some stars (Graziani *et al.*, 2014), while in the laboratory framework such conditions can be obtained for a few picoseconds only. In this case, the pump–probe scheme is routinely employed to heat a material up to eV temperatures (Rämer *et al.*, 2014) and study its properties before the hydrodynamic expansion ($\sim$10 ps after the pump pulse). In such a context, ultra-short and ultra-intense FEL pulses are a privileged tool, since they are not affected by plasma screening and can efficiently deposit energy in the material's bulk to achieve an isochoric heating. EIS-TIMEX has been designed

to maximize the FEL pump fluence by using an ellipsoidal mirror able to de-magnify the FEL spot down to 6 µm full width at half-maximum (FWHM). Before any experiment, a fast check of the focal plane and spot size is generally performed through single-shot damage on a YAG:Ce (yttrium aluminium garnet doped with cerium) screen, imaged using a Questar QM 100 microscope (see Fig. 1*b*). Using single-shot damage, it is possible to estimate the best spot dimension and its position with respect to the ellipsoidal mirror [Figs. 1(*c*) and 1(*d*)]. While YAG:Ce is useful to monitor and minimize the FEL spot, it is not the most appropriate material to precisely evaluate the FEL spot size. Nevertheless, the measured damage crater dimensions are in fairly good agreement with simulations, also confirmed by wavefront measurements (Zangrando *et al.*, 2015; Raimondi *et al.*, 2013, 2014). Moreover, it is worth stressing that this is only a quick procedure to check the focal plane position online. Once the focal plane has been identified, the same YAG:Ce screen is used to overlap spatially both the FEL pump and the optical laser probe pulses. Temporal superposition is usually estimated employing the measurement of the transient absorption induced by the FEL on selected samples. According to Durbin (2012), the FEL pulse can partially and transiently deplete the valence band of dielectric crystals, opening optical absorption channels otherwise forbidden. The obtained excited sample can then be probed by an optical laser, intrinsically synchronized (with an accuracy better than 10 fs) with the FEL emission (Danailov *et al.*, 2014). The transient absorption signal, below
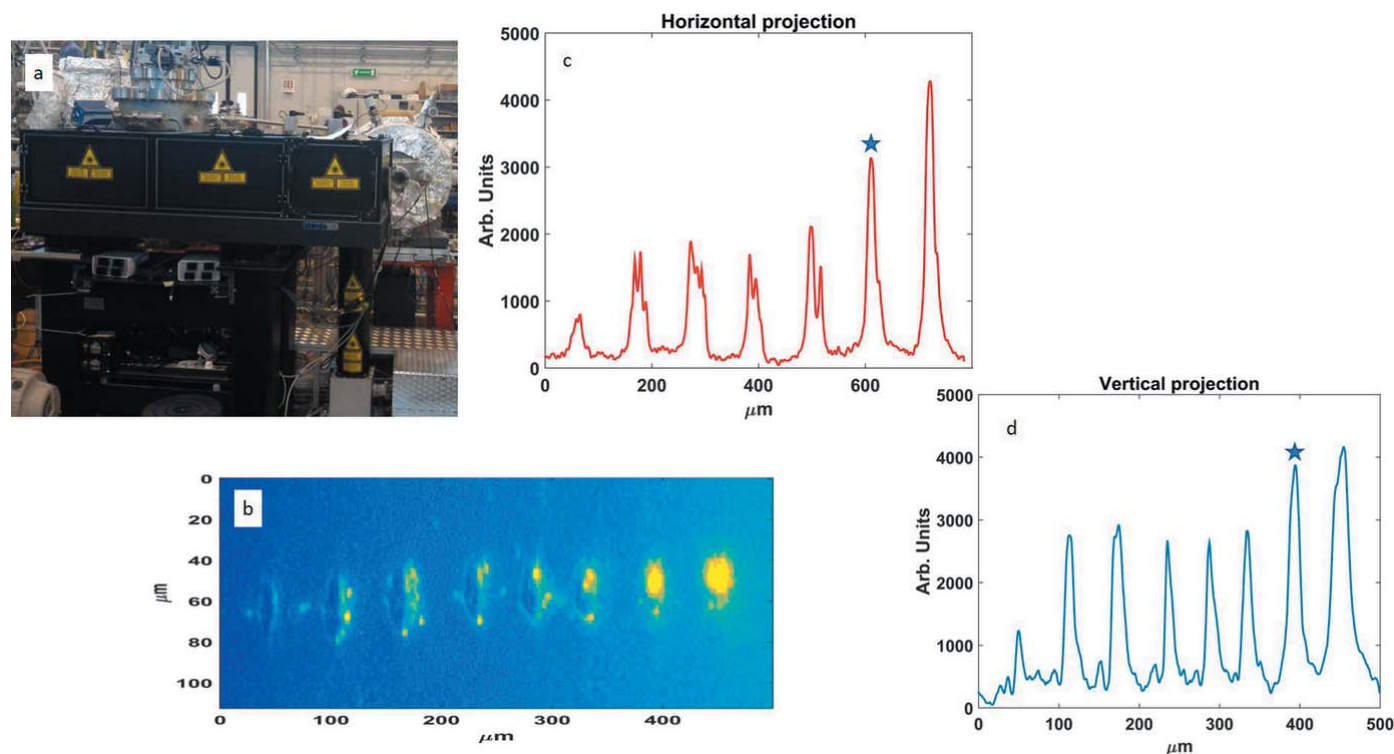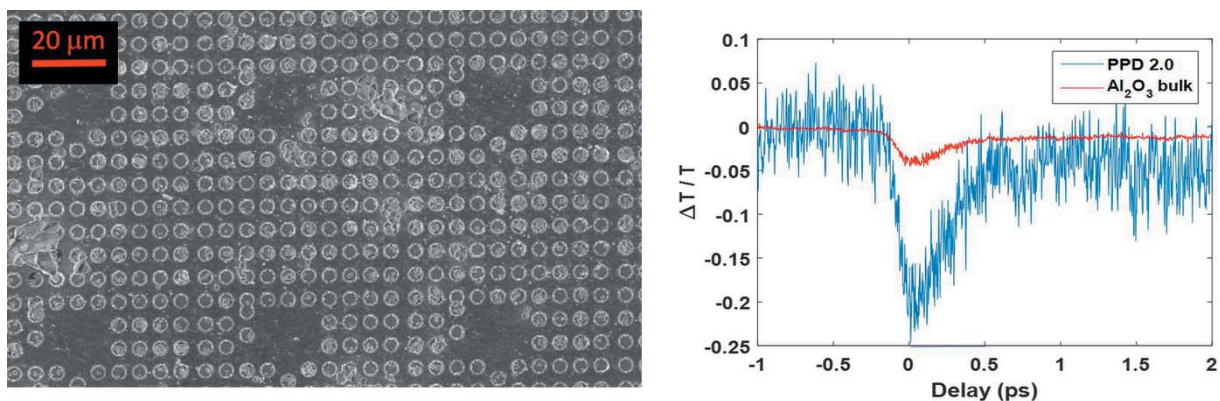

Figure 1
Panel (*a*) shows a photograph of the EIS-TIMEX endstation. In panel (*b*) the single-shot craters on the YAG:Ce are shown, obtained at different positions on the optical axis of the focusing ellipsoidal mirror. Panels (*c*) and (*d*) are the horizontal and vertical projections of the craters. The values of the projections are obtained by integrating the spots over the selected direction and merging the results in single graphs [panels (*c*) and (*d*)]. Stars indicate the smallest spot dimensions characterized by the smallest FWHM value.

the damage threshold of the material, is proportional to the FEL fluence (Casolari *et al.*, 2014). This, however, holds exactly only if the ratio between the FEL pump and optical probe spot size is ≥ 1. The setup available at EIS-TIMEX can provide optical laser spot sizes down to about 25 µm FWHM. Although the laser spot is relatively small, it is still bigger than typical FEL spots. This condition is unfavourable in order to obtain the desired contrast in FEL/pump–laser/probe measurements since the region of the laser spot which interacts with the FEL excited region of the sample is a fraction of the total laser spot area, which gives rise to a high baseline that weakens the contrast and can result in a difficult identification of t_0. Moreover, sample damage can be prevented only by keeping the FEL intensity low. Indeed, since the ellipsoidal mirror is an astigmatic element, it is not possible to obtain a homogeneous spot broadening by moving the sample along the optical axis of the mirror. Therefore, the fluence cannot be efficiently reduced by increasing the spot area. However, attenuating the FEL beam intensity finally affects the contrast between pumped and unpumped signals. These constraints demand for a purposely designed device to quickly and effectively achieve the temporal superposition of the two pulses. The device that we designed and realised is an evolution of the pixelated phosphor detector (PPD) presented elsewhere (Matruglio *et al.*, 2016). In this sample, we mixed the characteristics of the patterned phosphor, which facilitates the spatial overlapping of the pulses, with the 'timing' properties of a crystal. We call this new sample PPD 2.0. In this case, we choose Al_2O_3 as a substrate crystal onto which the phosphor wells and the timing zones were manufactured. The internal walls of the wells and the crystal surface have been coated with aluminium, except for some squared region comparable with the FEL spot dimension. This solution blocks the circular crown of the laser spot which is generally transmitted through an unexcited portion of the crystal. In such a manner, the baseline is strongly suppressed and the contrast in the measurement is enhanced, as shown in Fig. 2. More details about the fabrication process are given by Mincigrucci *et al.* (2016). To demonstrate the validity of the PPD approach we fixed the experimental conditions (FEL pump: 32 nm, esti-

mated pulse duration 50 fs, pulse energy at the source 1 µJ; infrared probe: 780 nm, pulse duration 100 fs, pulse energy 0.1 µJ). In such a way the total transmitted intensity is lower for the PPD and the detected signal compares with the electric noise. The signal-to-noise ratio is naturally decreased (from ~ 100 to ~ 10) but the original value may be recovered by increasing the probe pulse intensity and/or by using a better detector and/or averaging more (here we mention that each point of the traces represents a single shot). A simple UVG100 photodiode from OptoDiode was employed in the current case. The accurary of the method may be estimated, for example by the uncertainty in determining the position of the half drop, which, in the present case, is about 30 fs.

3. EIS-TIMER

EIS-TIMER is the FERMI endstation explicitly designed and built to perform transient grating (TG) experiments (Vega-Flick *et al.*, 2016; Bencivenga & Masciovecchio, 2009; Johnson *et al.*, 2012) in the mesoscopic region of the kinematical plane, *i.e.* in the 0.1–1 nm^{-1} wavevector range. In a TG experiment, two beams, the pumps, interfere at the sample position generating a standing electromagnetic wave. This wave couples to the system producing, among other excitations, a density wave with the same spatial periodicity as the transient grating. A third beam, the probe, impinges on the grating at the phase matching angle and it is diffracted off the grating toward the detector. The diffracted intensity as a function of time delay monitors the temporal evolution of the dynamics induced by the TG. The TG technique conjugated with the operative spectral range of FERMI represents a privileged tool for investigating the mesoscopic region. Indeed, in a TG experiment the wavevector (Q) of the stimulated excitations is given by $(4\pi \sin \theta)/\lambda$, where θ is the semi-angle between the pump beams and λ is the FEL pump wavelength. It is easy to see that different values of Q can be reached by varying θ and/or λ (Cucini *et al.*, 2011a). Phase matching can then be fulfilled by exploiting the third-harmonic content of the FERMI emission. Four different experimental geometries, corresponding to different values of θ, are available at the EIS-

Figure 2
Left: scanning electron microscopy view of the PPD 2.0. Right: transmission timing trace obtained with the bulk Al_2O_3 sample (red trace) and with the PPD 2.0 (blue trace) under the same experimental conditions.

TIMER beamline (Fig. 3). For further details, see Bencivenga *et al.* (2016). A first mirror (PrBS in Fig. 3) in the dedicated photon transport is employed as a wavefront-division beam-splitter. Half of the beam is steered (M1 and M2 in Fig. 3) toward a dedicated delay line (DL in Fig. 3) equipped with a set of multilayer mirrors working at incidence angles of 45°, in order to keep the dimension of the delay line compact while allowing for nanosecond-sized time delay scans.

The multilayers reflectivities are nominally peaked at around 17.8 nm, 13.3 nm, 6.7 nm and 3.3 nm and hence also allow for filtering out the first harmonic content from the probe beam. The maximum accessible time-delay range depends on the chosen geometries and varies between 3.5 ns (pump 1) and 1.5 ns (pump 4). In the end, the probe is steered toward the sample through a set of dedicated toroidal mirrors (PrsM in Fig. 3). The second half of the beam is split again by a second wavefront-division beam-splitter (PuBS in Fig. 3) and propagated toward the pump chambers. Each chamber contains a toroidal mirror which, if inserted, intercepts the beam and defines the pump trajectory (T1A, T1B, T2A, T2B in Fig. 3). Of the four available geometries (Cucini *et al.*, 2011*b*; Bencivenga *et al.*, 2016; Foglia *et al.*, 2017), only the first two have been commissioned (semi angle at the sample position of 9.2° and 13.8°) at the time of submitting this manuscript. Preliminary measurements of the pump spots, reported in Fig. 4, show that the focal spot dimensions estimated on a P20 (Weber, 2003) phosphorus screen are in quite good agreement with the simulations. However, further and more accurate studies are definitely needed to fully characterize the beams.

Due to the variety of the FEL trajectories and mechanical constraints inside the experimental chamber, it is not always possible to perform transient transmission or reflection measurements to determine t_0. Moreover, in TG experiments the temporal superposition between FEL and optical pulses is only a preliminary, yet critical, procedure. Indeed, the two FEL pump pulses have to be superposed in space and time to generate the TG, but due to the phase matching constraint the generation of the TG cannot be probed by an optical laser (*i.e.* the TG period is much shorter than optical wavelengths). In this framework, we ideated a new, fast and effective technique called 'crater scattering' (CS). In CS the main idea is to temporally increase the FEL intensity [usually removing some filters in the FEL transport path (Zangrando *et al.*, 2015) in order to slightly damage a flat Si_3N_4 surface]. The scattering of the optical laser (780 nm, 100 fs pulse duration and pulse energy of 0.1 µJ) from the surface is thus increased from nearly zero to a selectable value [Fig. 5(*a*), top and middle
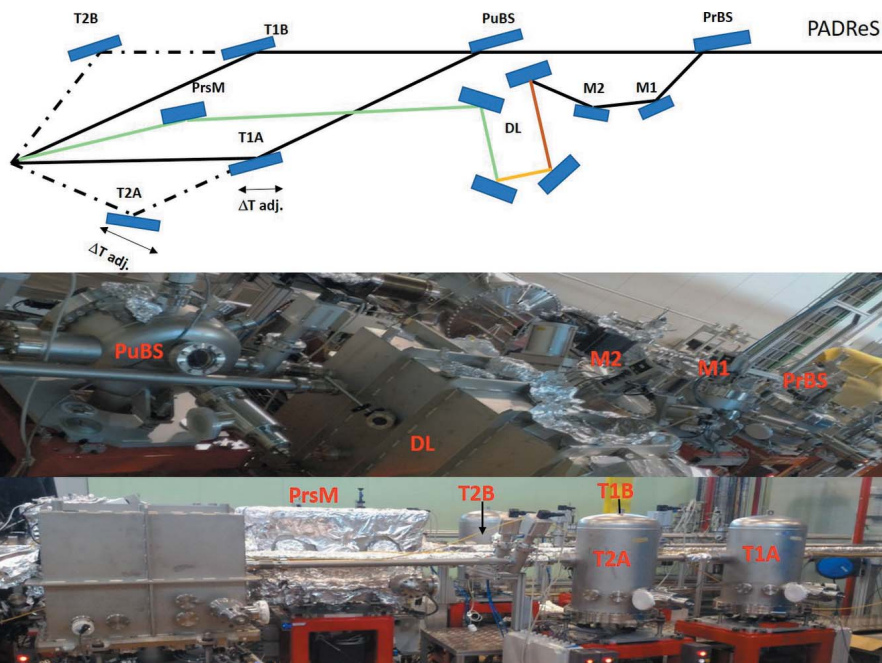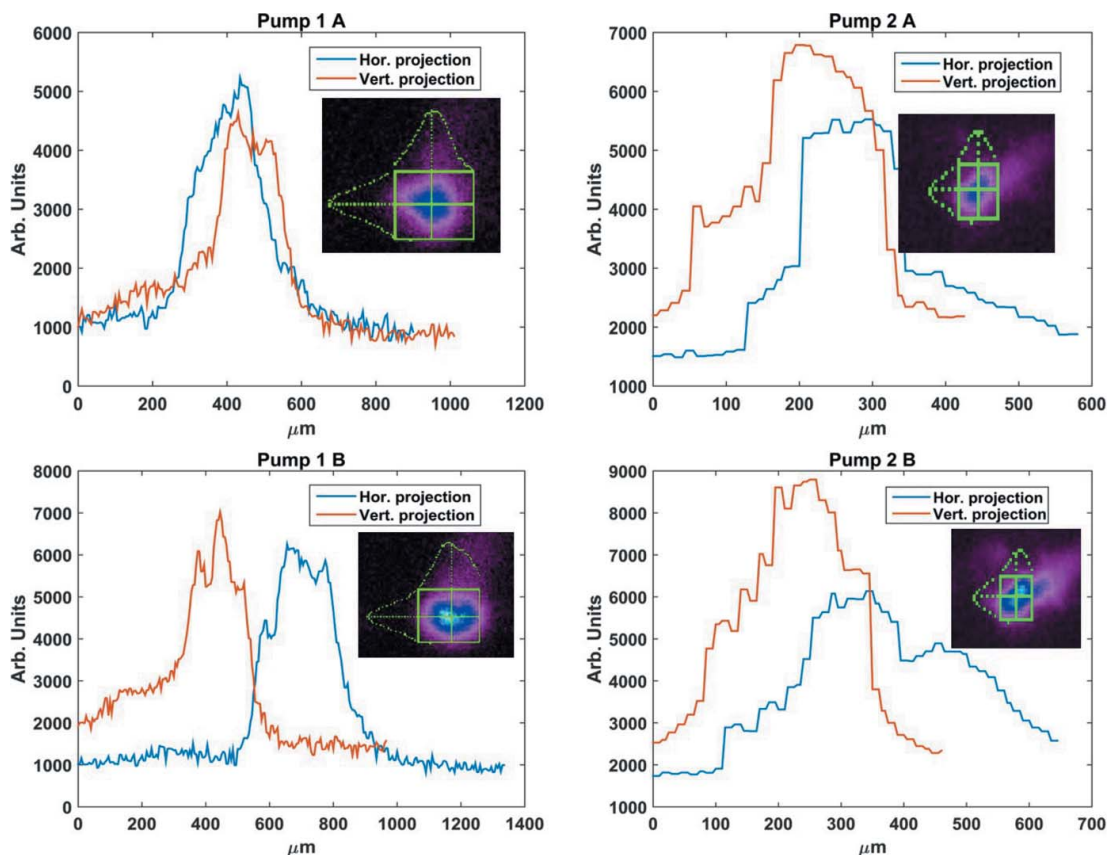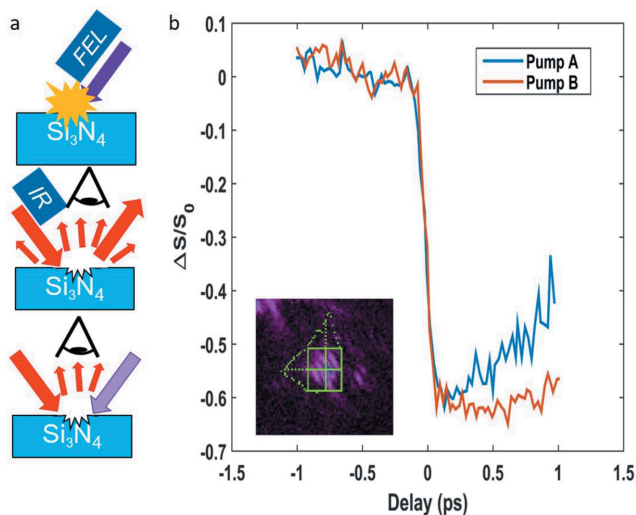

Figure 3
EIS-TIMER beamline.

diagrams]. In the subsequent step of the procedure the FEL intensity is decreased again to reach a fluence of ~10 mJ cm^{-2}. The FEL pulse had a central wavelength of 40 nm, an estimated time duration of 60 fs and an energy at the source of 10 µJ. This permits the system to be efficiently pumped without introducing any further variation of the surface morphology. Scanning the delay between the FEL and the optical pulse is possible to record a trace of the scattered intensity such as the ones shown in Fig. 5(*b*). In analogy with transient transmittivity/reflectivity experiments, t_0 can be defined as the time at which the half-drop in the scattered intensity occurs. According to Born *et al.* (1999), in a first-order approximation the scattered field is proportional to the spatial Fourier transform of $(\omega^2/4\pi c^2)(n^2 - 1)$, where ω is the pulsation of the probe field, c is the speed of light and n is the complex refractive index. Therefore, irrespective of the underlying physical processes, a FEL-induced modification of n (Durbin, 2012; Eckert *et al.*, 2015) results in a change of the total scattered intensity, in analogy with what is commonly observed in transient reflectivity or transmissivity experiments.

EIS-TIMER allows the optical pathlength of only one of the two pump beams to be varied, namely the A-branch. With such a constraint, the timing trace of the B-branch represents the reference trace and the goal of the temporal alignment is to superpose the A-branch trace to the reference one (see Fig. 5*b*). This is iteratively performed by moving the toroidal mirror in the A-branch along the trajectory of the reflected beam and correcting for deviations of the impinging point on the toroidal mirror and exit angle by using the pitch angles both of the toroidal mirror and of the pump beam splitter mirror. CS is a powerful technique under many aspects. First of all, it permits the base-line of the following transient scat-

Figure 4
Spot of the pump 1 and pump 2 trajectories. Estimated dimensions from the projections are: 200 μm × 180 μm (pump 1A, given by mirror T1A), 250 μm × 180 μm (pump 1B, given by mirror T1B), 150 μm × 170 μm (pump 2 A, given by mirror T2A), 200 μm × 180 μm (pump 2B, given by mirror T2B).

Figure 5
(*a*) Diagrams of the CS procedure. A FEL pulse with high intensity is employed to damage the Si_3N_4 surface (top, purple arrow). The scattering of an optical pulse from the crater is hence recorded by a CCD (middle and bottom). The FEL intensity is subsequently decreased (bottom, light purple arrow) and the transient scattered intensity measured. (*b*) Timing traces obtained with such a procedure, and an image of the scattering crater.

tering experiment to be defined in real time. Obtaining a low baseline is a key ingredient, as mentioned before, to reach a good contrast in the measurement. Secondly, it does not require a perfect alignment between the FEL pump and a well focused optical probe. In terms of time cost, this is a tremendous advantage, also considering the fact that the optical laser will not be used either as a pump or as probe in the subsequent TG experiments. Moreover, the crater behaves similarly to the pinhole discussed above. Starting from a perfectly flat surface, no photons are scattered toward the detector. Instead, the crater induces some photons to be scattered toward the detector, but only those showing an interaction with the crater itself. Since the crater is generated by the FEL, those photons surely originate from a FEL-excited region of the sample. To guarantee the maximum contrast, a crater per branch line is created. Furthermore, the detector employed in CS measurements is a low-cost commercial CCD camera coupled to a tele-microscope (Questar QM100). Directly imaging the surface permits the crater region to be precisely selected and the scattered intensity originating from the crater only to be integrated and measured (Fig. 5*b*). Due to its peculiarities, CS demonstrated to be a very efficient technique to determine t_0 and permitted a contrast in the measurement of up to 60% to be reached. Similarly to the case of the PPD 2.0 detection scheme (reported in §3), the uncertainty in the half-drop determina-

tion estimates the accuracy of the method in determining t_0 which is approximately 20 fs in the present case.

4. DiProI

DiProI is a multi-purpose endstation. It is equipped with Kirkpatrick–Baez mirrors able to independently focus the FEL beam in the horizontal and vertical direction. The DiProI system uniqueness resides in the fact that the two mirrors are bendable. This enables the FEL spot size to be varied from a few μm^2 to a few mm^2; for major details see Capotondi *et al.* (2013, 2015) and Raimondi (2017). Thanks to its flexibility and re-configurability, DiProI can host a number of setups: they can range from the mini-TIMER setup (Bencivenga *et al.*, 2015) to diffraction imaging (Willems *et al.*, 2017; Martin *et al.*, 2014). As with the other above-mentioned endstations, DiProI is equipped with an optical probing laser, intrinsically synchronized with the FEL emission (Danailov *et al.*, 2014). Three possible trajectories for the laser are available: 2°, 15° and 45°. Angles are given with respect to the FEL beam. In order to determine t_0 in DiProI, thanks to the possibility to vary (enlarge) the FEL spot and to match the laser spot size (100 μm FWHM), it is not required to adopt particular strategies to control the effective interaction region and the standard transient reflectivity/transmittivity measurements are more than appropriate. The laser was characterized by a central wavelength of 780 nm, a time duration of 100 fs and a pulse energy of 0.5 μJ. The easiness in determining the time instant at which the pulses overlap permitted more advanced studies on the physical process behind the phenomenon to be performed. To this end (see Fig. 6), we installed a setup to measure the polarization of the reflected/transmitted light both in reflection and in transmission geometry. In both geometries, the first element of the setup is a wave plate used to obtain a balanced signal after the Wollaston prism that separates the horizontal and vertical polarization components. The two linearly polarized beams, emerging from the prism, have been detected making use of an optical bridge, consisting of a couple of nominally identical photodiodes (Thorlabs PDB210A).

A beam splitter installed before the Wollaston prism (not shown in Fig. 6) completes the setup. Its purpose is to steer a small fraction of the beam (~5%) to a commercial CCD camera (Basler Scout), to have a reference for the beam pointing, in addition to a redundant determination of the total reflected/transmitted intensity. The same detection scheme is employed both in reflection and in transmission geometry. In this preliminary study, the setup was used to investigate a diamond crystal (8 mm × 8 mm × 1.5 mm chemical vapour deposition single-crystal plate, face orientation along the ⟨100⟩ direction, nitrogen and boron concentration below 1 part per million, both faces with a roughness below 30 nm r.m.s.), as a function of the FEL fluence. The central FEL wavelength was 25 nm and the estimated time duration 50 fs. Before any measurement the half-wave plate was slightly rotated to balance the polarizations and obtain a zero difference in the optical bridge. Diamond shows a peculiar signal already in the
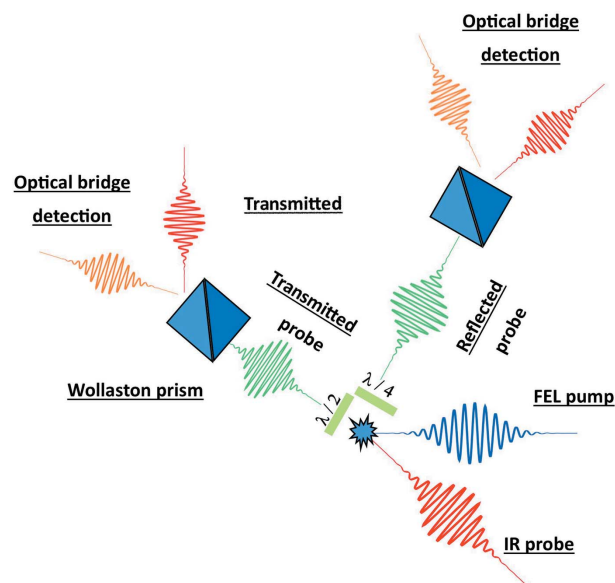
Figure 6
Sketch of the polarization-sensitive optical setup installed at the DiProI endstation for performing polarization-resolved transient reflectivity/ transmittivity experiments.

polarization-insensitive transmission trace (see Fig. 7). The signal is characterized by a fast increase of the transmission at t_0, suddenly followed (250 fs) by a decrease of the same magnitude (10%) with a slower recovery (picosecond time scale). A similar behaviour persists in the polarization difference trace. The accuracy in the estimation of t_0 varies from approximately 140 fs in the lowest fluence case (4 mJ cm^{-2}) to about 70 fs in the highest fluence case (27 mJ cm^{-2}). On the contrary, in reflection geometry the polarization-independent time traces show a smooth trend characterized by a fast decrease of the reflectivity (~500 fs) and a slower recovery (~ps). However, a more careful analysis of the polarization difference trace highlights a trend resembling the one found in transmission. Similar values for the accuracy in the reflection geometry have been observed. The first steps in the data interpretation of reflectivity and transmittivity traces are being conducted in the framework of a density-dependent two-temperature model (nTTM) (Rämer *et al.*, 2014). The set of differential equations defined in the nTTM, which describes the time evolution of electron density and of carrier and lattice temperatures, are being used to describe the interaction of the FEL pump with the diamond crystal. The absorption of FEL photons transiently alters the free-electron density, as well as both the electronic and lattice temperatures, hence transiently modifying the complex refraction index of the material in a layer with thickness comparable with the FEL penetration length. At the highest fluence (27 mJ cm^{-2}), the free-electron density can reach a value of $\sim 1 \times 10^{21}$ e$^-$ cm^{-3}, accompanied by a peak electron temperature of ~10 eV. The electron subsystem couples with the lattice subsystem reaching an equilibrium temperature (0.05 eV) with the ions in ~100 fs. The alteration of the optical constants is significant: at t_0 the real part is modified by about 10% while the imaginary part, related to the absorption, reaches a maximum value of 0.2.
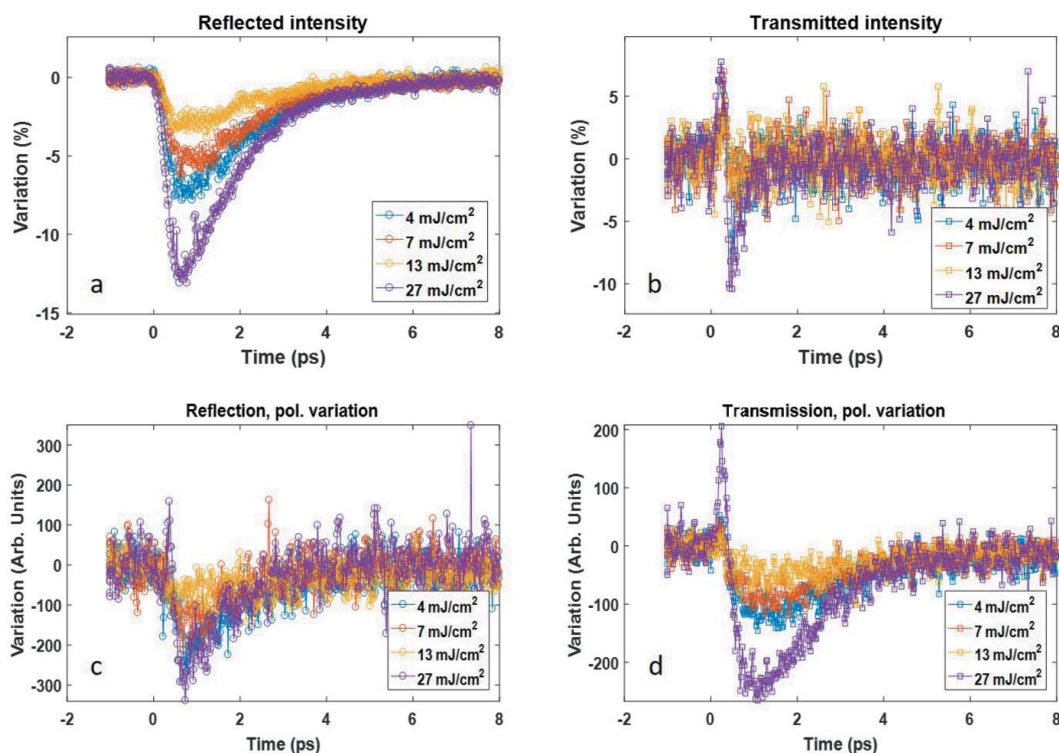
Figure 7
Time-resolved traces for the total reflected (*a*) and transmitted (*b*) intensity. Panels (*c*) and (*d*) refer to the polarization change for the reflected and transmitted beams.

A variety of non-linear phenomena arising from pulse propagation can take place in a medium with non-constant optical parameters (Boyd, 1996; Lebedev *et al.*, 2005; Wahl-strand *et al.*, 2013). Therefore, data analysis and interpretation are not straightforward and are still ongoing. Nevertheless, in the optical spectral window similar phenomena have been observed for example using an IR pump and a super-continuum probe. The alteration of the optical constants due to the pump can induce a time-dependent energy redistribution among the spectral components of the probe. Similar shapes have been observed in a transmission geometry (Ekvall *et al.*, 2000). This phenomenon is known as cross phase modulation. Qualitatively, it can be explained recalling the fact that a pulse propagating in a non-linear medium can experience a modification of its temporal profile (*e.g.* a pulse steepening) which introduces more spectral components on the 'head' of the pulse that can interfere with the already present ones. Quantification of this phenomenon is strictly related to the precise measurement/knowledge of the chirp of the pulses. Similarly, a more complete description of the pulse propagation can contemplate also a rotation of the polarization which can ultimately describe our trend in the polarization variation. This generally happens at time scales comparable with the pulse length ($\sim$100–200 fs). At longer time scales, the persistence of a negative value in the signal may simply indicate the persistence of the FEL opened absorption channel, and can give an estimation of the recombination lifetimes of the carriers. However, the magnitude of the effect can be modified by interferential effects. As a conclusive remark, it is important to stress that the vast majority of similar studies in the visible energy regime have been conducted in a transparent medium, an approximation which is not true in our specific case.

5. Conclusion

The main characteristics of the FEL spots for the EIS-TIMEX, EIS-TIMER and DiProI endstations have been introduced and their advantages/disadvantages regarding the timing diagnostics have been discussed. A pixelated detector developed to increase the experimental sensitivity in the timing procedure at the EIS-TIMEX beamline was introduced. The same approach can be employed as well to perform non-destructive pump–probe experiments. Moreover, the pixelated detector merges the capabilities of a phosphor screen and of a timing crystal, resulting in time and space saving. The CS technique was developed at the EIS-TIMER endstation and enables a very fast and effective timing, without the need of a precise spatial overlap of the FEL and IR beam. The CS technique can be easily extended in any other endstation equipped with a tele-microscope. DiProI possesses the capability of adjusting the FEL shape and can easily match, if needed, the optical focal spot. Alongside its extreme flexibility, this enables DiProI to be a privileged tool to straightforwardly perform non-destructive pump–probe measurements. In this framework we conducted polarization-resolved timing experiments, the analysis of which is still ongoing.

References

Allaria, E., Appio, R., Badano, L., Barletta, W. A., Bassanese, S., Biedron, S. G., Borga, A., Busetto, E., Castronovo, D., Cinquegrana, P., Cleva, S., Cocco, D., Cornacchia, M., Craievich, P., Cudin, I., D'Auria, G., Dal Forno, M., Danailov, M. B., De Monte, R., De Ninno, G., Delgiusto, P., Demidovich, A., Di Mitri, S., Diviacco, B., Fabris, A., Fabris, R., Fawley, W., Ferianis, M., Ferrari, E., Ferry, S., Froehlich, L., Furlan, P., Gaio, G., Gelmetti, F., Giannessi, L., Giannini, M., Gobessi, R., Ivanov, R., Karantzoulis, E., Lonza, M., Lutman, A., Mahieu, B., Milloch, M., Milton, S. V., Musardo, M., Nikolov, I., Noe, S., Parmigiani, F., Penco, G., Petronio, M., Pivetta, L., Predonzani, M., Rossi, F., Rumiz, L., Salom, A., Scafuri, C., Serpico, C., Sigalotti, P., Spampinati, S., Spezzani, C., Svandrlik, M., Svetina, C., Tazzari, S., Trovo, M., Umer, R., Vascotto, A., Veronese, M., Visintini, R., Zaccaria, M., Zangrando, D. & Zangrando, M. (2012). *Nat. Photon.* **6**, 699–704.

Bencivenga, F., Cucini, R., Capotondi, F., Battistoni, A., Mincigrucci, R., Giangrisostomi, E., Gessini, A., Manfredda, M., Nikolov, I. P., Pedersoli, E., Principi, E., Svetina, C., Parisse, P., Casolari, F., Danailov, M. B., Kiskinova, M. & Masciovecchio, C. (2015). *Nature (London)*, **520**, 205–208.

Bencivenga, F. & Masciovecchio, C. (2009). *Nucl. Instrum. Methods Phys. Res. A*, **606**, 785–789.

Bencivenga, F., Zangrando, M., Svetina, C., Abrami, A., Battistoni, A., Borghes, R., Capotondi, F., Cucini, R., Dallari, F., Danailov, M., Demidovich, A., Fava, C., Gaio, G., Gerusina, S., Gessini, A., Giacuzzo, F., Gobessi, R., Godnig, R., Grisonich, R., Kiskinova, M., Kurdi, G., Loda, G., Lonza, M., Mahne, N., Manfredda, M., Mincigrucci, R., Pangon, G., Parisse, P., Passuello, R., Pedersoli, E., Pivetta, L., Prica, M., Principi, E., Rago, I., Raimondi, L., Sauro, R., Scarcia, M., Sigalotti, P., Zaccaria, M. & Masciovecchio, C. (2016). *J. Synchrotron Rad.* **23**, 132–140.

Beye, M., Sorgenfrei, F., Schlotter, W. F., Wurth, W. & Föhlisch, A. (2010). *Proc. Natl Acad. Sci. USA*, **107**, 16772–16776.

Born, M., Wolf, E. & Bhatia, A. B. (1999). *Principles of Optics: Electromagnetic Theory of Propagation, Interference and Diffraction of Light.* Cambridge University Press.

Borrego-Varillas, R., Oriana, A., Ganzer, L., Trifonov, A., Buchvarov, I., Manzoni, C. & Cerullo, G. (2016). *Opt. Express*, **24**, 28491–28499.

Boyd, R. (1996). *Nonlinear Optics.* New York: Academic Press.

Capotondi, F., Pedersoli, E., Bencivenga, F., Manfredda, M., Mahne, N., Raimondi, L., Svetina, C., Zangrando, M., Demidovich, A., Nikolov, I., Danailov, M., Masciovecchio, C. & Kiskinova, M. (2015). *J. Synchrotron Rad.* **22**, 544–552.

Capotondi, F., Pedersoli, E., Mahne, N., Menk, R. H., Passos, G., Raimondi, L., Svetina, C., Sandrin, G., Zangrando, M., Kiskinova, M., Bajt, S., Barthelmess, M., Fleckenstein, H., Chapman, H. N., Schulz, J., Bach, J., Frömter, R., Schleitzer, S., Müller, L., Gutt, C. & Grübel, G. (2013). *Rev. Sci. Instrum.* **84**, 051301.

Casolari, F., Bencivenga, F., Capotondi, F., Giangrisostomi, E., Manfredda, M., Mincigrucci, R., Pedersoli, E., Principi, E., Masciovecchio, C. & Kiskinova, M. (2014). *Appl. Phys. Lett.* **104**, 191104.

Cucini, R., Bencivenga, F. & Masciovecchio, C. (2011a). *Opt. Lett.* **36**, 1032–1034.

Cucini, R., Bencivenga, F., Zangrando, M. & Masciovecchio, C. (2011b). *Nucl. Instrum. Methods Phys. Res. A*, **635**, S69–S74.

Cucini, R., Taschin, A., Ziparo, C., Bartolini, P. & Torre, R. (2007). *Eur. Phys. J. Spec. Top.* **141**, 133–136.

Danailov, M. B., Bencivenga, F., Capotondi, F., Casolari, F., Cinquegrana, P., Demidovich, A., Giangrisostomi, E., Kiskinova, M. P., Kurdi, G., Manfredda, M., Masciovecchio, C., Mincigrucci, R., Nikolov, I. P., Pedersoli, E., Principi, E. & Sigalotti, P. (2014). *Opt. Express*, **22**, 12869–12879.

Durbin, S. M. (2012). *AIP Adv.* **2**, 042151.

Eckert, S., Beye, M., Pietzsch, A., Quevedo, W., Hantschmann, M., Ochmann, M., Ross, M., Minitti, M. P., Turner, J. J., Moeller, S. P., Schlotter, W. F., Dakovski, G. L., Khalil, M., Huse, N. & Föhlisch, A. (2015). *Appl. Phys. Lett.* **106**, 061104.

Ekvall, K., van der Meulen, P., Dhollande, C., Berg, L.-E., Pommeret, S., Naskrecki, R. & Mialocq, J.-C. (2000). *J. Appl. Phys.* **87**, 2340–2352.

Foglia, L., Bencivenga, F., Mincigrucci, R., Simoncig, A., Calvi, A., Cucini, R., Principi, E., Zangrando, M., Mahne, N., Manfredda, M., Raimondi, L., Pedersoli, E., Capotondi, F., Kiskinova, M. & Masciovecchio, C. (2017). *Proc. SPIE*, **10237**, 102370C.

Graziani, F., Desjarlais, M. P., Redmer, R. & Trickey, S. B. (2014). *Frontiers and Challenges in Warm Dense Matter*, Vol. 96 of *Lecture Notes in Computational Science and Engineering.* Berlin: Springer.

Gutt, C., Sant, T., Ksenzov, D., Capotondi, F., Pedersoli, E., Raimondi, L., Nikolov, I. P., Kiskinova, M., Jaiswal, S., Jakob, G., Kläui, M., Zabel, H. & Pietsch, U. (2017). *Struct. Dyn.* **4**, 055101.

Harmand, M., Coffee, R., Bionta, M. R., Chollet, M., French, D., Zhu, D., Fritz, D. M., Lemke, H. T., Medvedev, N., Ziaja, B., Toleikis, S. & Cammarata, M. (2013). *Nat. Photon.* **7**, 215–218.

Johnson, J. A., Maznev, A. A., Bulsara, M. T., Fitzgerald, E. A., Harman, T. C., Calawa, S., Vineis, C. J., Turner, G. & Nelson, K. A. (2012). *J. Appl. Phys.* **111**, 023503.

Kowalewski, M., Bennett, K., Dorfman, K. E. & Mukamel, S. (2015). *Phys. Rev. Lett.* **115**, 193003.

Kruglik, S. G., Lambry, J. C., Martin, J. L., Vos, M. H. & Negrerie, M. (2011). *J. Raman Spectrosc.* **42**, 265–275.

Lebedev, M. V., Misochko, O. V., Dekorsy, T. & Georgiev, N. (2005). *J. Exp. Theor. Phys.* **100**, 272–282.

Martin, A. V., D'Alfonso, A. J., Wang, F., Bean, R., Capotondi, F., Kirian, R. A., Pedersoli, E., Pedersoli, E., Raimondi, L., Stellato, F., Yoon, C. H. & Chapman, H. N. (2014). *Nat. Commun.* **5**, 4661.

Matruglio, A., Dal Zilio, S., Sergo, R., Mincigrucci, R., Svetina, C., Principi, E., Mahne, N., Raimondi, L., Turchet, A., Masciovecchio, C., Lazzarino, M., Cautero, G. & Zangrando, M. (2016). *J. Synchrotron Rad.* **23**, 29–34.

Mincigrucci, R., Matruglio, A., Calvi, A., Foglia, L., Principi, E., Simoncig, A., Bencivenga, F., Dallorto, S., Gessini, A., Kurdi, G., Olynick, D., Dhuey, S., Sergo, R., Lazzarino, M., Masciovecchio, C. & Zilio, S. D. (2016). *Opt. Lett.* **41**, 5090–5093.

Raimondi, L., Svetina, C., Mahne, N., Cocco, D., Abrami, A., De Marco, M., Fava, C., Gerusina, S., Gobessi, R., Capotondi, F., Pedersoli, E., Kiskinova, M., De Ninno, G., Zeitoun, P., Dovillaire, G., Lambert, G., Boutu, W., Merdji, H., Gonzalez, A. I., Gauthier, D. & Zangrando, M. (2013). *Nucl. Instrum. Methods Phys. Res. A*, **710**, 131–138.

Raimondi, L., Svetina, C., Mahne, N., Cocco, D., Capotondi, F., Pedersoli, E., Manfredda, M., Kiskinova, M., Keitel, B., Brenner, G., Plönjes, E., Mey, T., Mann, K. & Zangrando, M. (2014). *Proc. SPIE*, **9208**, 920804.

Rämer, A., Osmani, O. & Rethfeld, B. (2014). *J. Appl. Phys.* **116**, 053508.

Vega-Flick, A., Duncan, R. A., Eliason, J. K., Cuffe, J., Johnson, J. A., Peraud, J. P. M., Zeng, L., Lu, Z., Maznev, A. A., Wang, E. N., Alvarado-Gil, J. J., Sledzinska, M., Sotomayor Torres, C. M., Chen, G. & Nelson, K. A. (2016). *AIP Adv.* **6**, 121903.

Wahlstrand, J. K., Odhner, J. H., McCole, E. T., Cheng, Y. H., Palastro, J. P., Levis, R. J. & Milchberg, H. M. (2013). *Phys. Rev. A*, **87**, 053801.

Weber, M. J. (2003). *Handbook of Optical Materials.* Boca Raton: CRC Press.

Willems, F., von Korff Schmising, C., Weder, D., Günther, C. M., Schneider, M., Pfau, B., Meise, S., Guehrs, E., Geilhufe, J., Merhe, A. E. D., Jal, E., Vodungbo, B., Lüning, J., Mahieu, B., Capotondi, F., Pedersoli, E., Gauthier, D., Manfredda, M. & Eisebitt, S. (2017). *Struct. Dyn.* **4**, 014301.

Zangrando, M., Cocco, D., Fava, C., Gerusina, S., Gobessi, R., Mahne, N., Mazzucco, E., Raimondi, L., Rumiz, L. & Svetina, C. (2015). *J. Synchrotron Rad.* **22**, 565–570.